

## CATALYSIS

# Restructuring of titanium oxide overlayers over nickel nanoparticles during catalysis

Matteo Monai<sup>1†</sup>, Kellie Jenkinson<sup>2†</sup>, Angela E. M. Melcherts<sup>1†</sup>, Jaap N. Louwen<sup>1</sup>, Ece A. Irmak<sup>2</sup>, Sandra Van Aert<sup>2</sup>, Thomas Altantzis<sup>3</sup>, Charlotte Vogt<sup>1†</sup>, Ward van der Stam<sup>1</sup>, Tomáš Duchoň<sup>4</sup>, Břetislav Šmíd<sup>5</sup>, Esther Groeneveld<sup>6</sup>, Peter Berben<sup>6</sup>, Sara Bals<sup>2\*</sup>, Bert M. Weckhuysen<sup>1\*</sup>

Reducible supports can affect the performance of metal catalysts by the formation of suboxide overlayers upon reduction, a process referred to as the strong metal–support interaction (SMSI). A combination of operando electron microscopy and vibrational spectroscopy revealed that thin TiO<sub>x</sub> overlayers formed on nickel/titanium dioxide catalysts during 400°C reduction were completely removed under carbon dioxide hydrogenation conditions. Conversely, after 600°C reduction, exposure to carbon dioxide hydrogenation reaction conditions led to only partial reexposure of nickel, forming interfacial sites in contact with TiO<sub>x</sub> and favoring carbon–carbon coupling by providing a carbon species reservoir. Our findings challenge the conventional understanding of SMSIs and call for more-detailed operando investigations of nanocatalysts at the single-particle level to revisit static models of structure–activity relationships.

Supported metal catalysts respond to pretreatment and reaction conditions by restructuring (1), phase changes (2), and chemical and structural oscillations (3), which can lead to catalyst activation, deactivation, or changes in selectivity. A good example of catalyst restructuring is the so-called strong metal–support interaction (SMSI), in which metal nanoparticles (NPs) are encapsulated by overlayers of reducible supports, such as TiO<sub>2</sub>, after high-temperature reduction (4) or oxidation (5). SMSI can result in a substantial change in product selectivity (6), and it has been shown to be correlated with high activity of mixed metal oxides in the oxygen evolution reaction (7) and with activation of industrial Cu/ZnO<sub>x</sub>/Al<sub>2</sub>O<sub>3</sub> catalysts (8).

Although there is substantial evidence for overlayer formation during catalyst pretreatments (9–11), including from atomic-resolution in situ electron microscopy studies of overlayer formation under H<sub>2</sub> (10, 12–14), O<sub>2</sub> (5), and CO<sub>2</sub> environments (14), very little is known about the structure of the overlayer under reaction conditions. Recently, the complete removal of a TiO<sub>x</sub> (x ≤ 2) overlayer was shown for Pt/TiO<sub>2</sub> using in situ transmission electron microscopy

(TEM) under O<sub>2</sub>/H<sub>2</sub> mixtures at 600°C (12). This result raises the question of whether overlayers persist during reaction conditions or if the pretreatments used to induce SMSI only indirectly affect the catalyst performance, for example, by particle growth or phase changes, given that the geometric and electronic structure of prereduced catalysts can change substantially under reaction conditions (15, 16). Multiscale operando methodologies (from single nanoparticle to ensemble level) are crucial to develop meaningful structure–performance relations for supported metal NPs. Recent advances in high-resolution TEM methods allow the observation of materials under operando conditions at ambient pressure and at high temperatures relevant to catalysis (17–19).

Here, we unravel the evolution of TiO<sub>x</sub> overlayers on industrially relevant Ni/TiO<sub>2</sub> catalysts during catalysis, for the CO and CO<sub>2</sub> hydrogenation reaction, after low-temperature (400°C) and high-temperature (600°C) reduction. We combined quantitative operando scanning TEM (STEM) and infrared (IR) spectroscopy, near-ambient pressure x-ray photoelectron spectroscopy (NAP-XPS), and density functional theory (DFT) calculations to observe and understand overlayer restructuring and its effect on catalysis. The combination of both nano- and bulk-scale operando analytical techniques reveals information with unprecedented resolution on the single-atom level and also provides new insights into the properties of the ensemble of supported metal nanoparticles.

We show that TiO<sub>x</sub> overlayers, formed during reduction, restructure in CO<sub>2</sub>/H<sub>2</sub> mixtures at a temperature as low as 200°C, (partially) reexposing the Ni surface and introducing interfacial sites responsible for higher C–C coupling activity. We tailored suboxide over-

layers to be stable under reaction conditions using different reduction pretreatment temperatures. This capability adds a parameter for catalyst optimization. These results could enable an understanding of the performance of a number of supported metals in reactions for sustainable technologies, such as biomass upgrading (20) and CO<sub>2</sub> valorization (21, 22).

## Ni partial encapsulation during 400°C reduction

To induce oxide overlayer coverage by SMSI and to investigate its role in CO<sub>2</sub> hydrogenation, we reduced 6 wt % Ni/TiO<sub>2</sub> catalysts at 400°C (400-Ni/TiO<sub>2</sub>). The formation of TiO<sub>x</sub> overlayers upon the supported Ni NPs was investigated on the single-particle level by in situ electron microscopy experiments in a windowed gas cell (climate G+, gas supply system, DENSSolutions) (Fig. 1A; see the supplementary materials for details). In situ reduction of Ni/TiO<sub>2</sub> at 400°C yielded supported metallic Ni NPs with an average diameter of 7.4 nm, and a size distribution of ±1.5 nm SD (Fig. 1B and figs. S4 and S5) that were consistent with STEM and x-ray diffraction (XRD) observations after ex situ reduction (figs. S8 and S9 and tables S1 and S2). The metallic state of the Ni NPs was confirmed by the Fourier transforms derived from the atomic-resolution high-angle annular dark-field scanning transmission electron microscopy (HAADF-STEM) images (figs. S10 and S11).

A TiO<sub>x</sub> overlayer was detected on Ni NPs by in situ HAADF-STEM imaging for 400-Ni/TiO<sub>2</sub> that corresponded to a partially encapsulating bilayer (Fig. 1C and figs. S12 and S13). This bilayer formed preferentially over (111) Ni surfaces for each of the five Ni NPs observed in a crystallographic zone axis, with no evidence of overlayer formation on other Ni facets (figs. S12 and S13). Because we aimed to investigate the catalyst dynamics in H<sub>2</sub> and during CO/CO<sub>2</sub> methanation conditions, it was important that structural changes that we observed were not an artifact of the electron beam. Therefore, we acquired multiple frames of the encapsulated Ni NP with low screen currents and fast image acquisition parameters to minimize potential electron beam–induced artifacts (23). After applying neural network restoration of the HAADF-STEM data and frame averaging, we could estimate the positions of the atomic columns with high accuracy and precision. We applied statistical parameter estimation theory to determine and refine the atomic column positions in the Ni NP and in the two atomic layers of Ti (Fig. 1D and figs. S14 to S16) (24). In addition, we applied the more-advanced maximum a posteriori probability rule to detect the Ti overlayer atomic columns that yield low contrast-to-noise ratio (25, 26).

Next, the displacements of all atomic columns with respect to the ideal atomic column

<sup>1</sup>Inorganic Chemistry and Catalysis Group, Institute for Sustainable and Circular Chemistry and Debye Institute for Nanomaterials Science, Utrecht University, 3584 CG Utrecht, Netherlands. <sup>2</sup>EMAT and NANOLab Center of Excellence, University of Antwerp, 2020 Antwerp, Belgium. <sup>3</sup>ELCAT, University of Antwerp, 2610 Wilrijk, Belgium. <sup>4</sup>Peter-Grünberg-Institut 6, Forschungszentrum Jülich GmbH, 52425 Jülich, Germany. <sup>5</sup>Department of Surface and Plasma Science, Faculty of Mathematics and Physics, Charles University, 180 00 Prague, Czech Republic. <sup>6</sup>BASF Nederland B.V., 3454 PK De Meern, Netherlands.

\*Corresponding author. Email: Sara.Bals@uantwerpen.be (S.B.); B.M.Weckhuysen@uu.nl (B.M.W.)

†These authors contributed equally to this work.

‡Present address: Schulich Faculty of Chemistry, Technion, Israel Institute of Technology, Technion City, Haifa 32000, Israel.

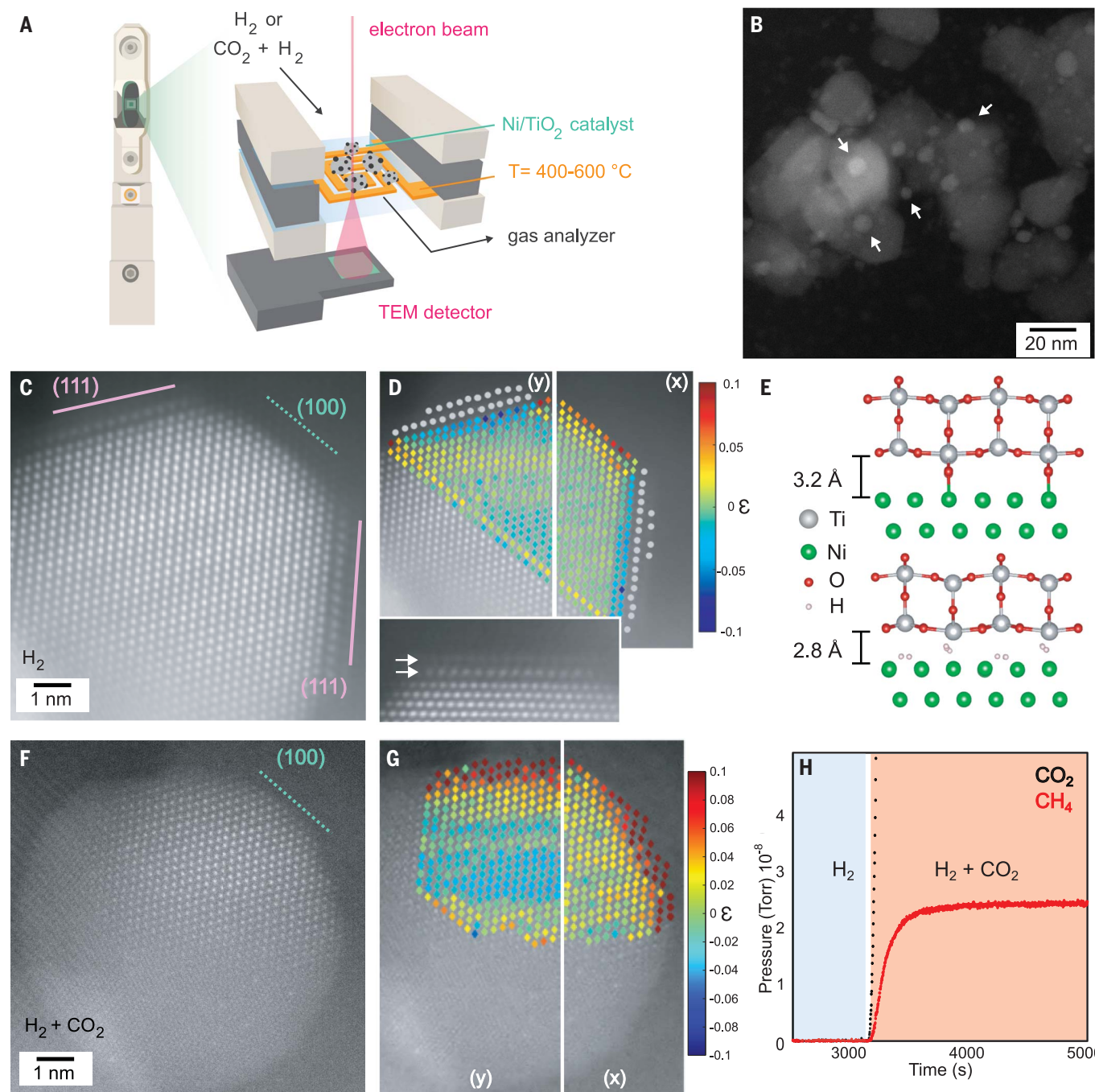


**Fig. 1.  $\text{TiO}_x$  overlayer formation by low-temperature  $\text{H}_2$  reduction and its restructuring during  $\text{CO}_2$  methanation on a  $\text{Ni/TiO}_2$  hydrogenation catalyst.**

(A) Schematic of the operando electron microscopy setup and windowed gas cell (climate G+, DENSolutions) used in this study. (B) HAADF-STEM overview image of a  $\text{Ni/TiO}_2$  catalyst prepared in situ at  $400^\circ\text{C}$  ( $400\text{-Ni/TiO}_2$ ), where white arrows highlight the Ni NPs upon the  $\text{TiO}_2$  support. (C) Representative atomic-resolution HAADF-STEM image of a Ni NP in a  $\text{Ni/TiO}_2$  catalyst in  $\text{H}_2$  at  $400^\circ\text{C}$ . Solid lines indicate  $\text{TiO}_x$ -covered Ni atomic planes, and dashed lines indicate unoccupied facets. Ni(111) and Ni(100) facets are indicated by pink and green, respectively. (D) Estimated positions of Ti (gray) and Ni (color scale) atomic columns. Ni atomic columns were identified through statistical parameter estimation theory and neural network image restoration, and Ti atomic positions were identified using a combination of statistical parameter estimation theory and MAP probability rule because of Ti's limited visibility (25, 26). Strain maps (resulting from the displacements with respect to the ideal

atomic column positions) in the x and y directions. Inset: Close-up of the  $\text{TiO}_x$  bilayer, where white arrows highlight each Ti layer. (E) Model of rutile  $\text{TiO}_2$  (110) overlayer on a Ni(111) slab with oxygen (top) or hydrogen (bottom) atoms occupying the Ni-Ti interface calculated by DFT, suggesting that the titania overlayer is partially reduced at the interface. (F) HAADF-STEM image of the same particle as in (D) upon exposure to a  $\text{CO}_2/\text{H}_2$  (0.25 bar: 0.75 bar) mixture at  $400^\circ\text{C}$  showing complete reexposure of Ni and NP restructuring. (G) Estimated atomic column positions of Ni from the same particle shown in (F) identified through statistical parameter estimation theory and neural network image restoration. Strain maps in the x and y directions resulting from the displacements with respect to the ideal atomic column positions. (H) MS data measuring the partial pressure of  $\text{CO}_2$  (black) and  $\text{CH}_4$  (red) for the  $\text{Ni/TiO}_2$  catalysts at  $400^\circ\text{C}$ . Regions highlighted in light blue and pink correspond to  $\text{H}_2$  and  $\text{CO}_2/\text{H}_2$  environments, respectively.



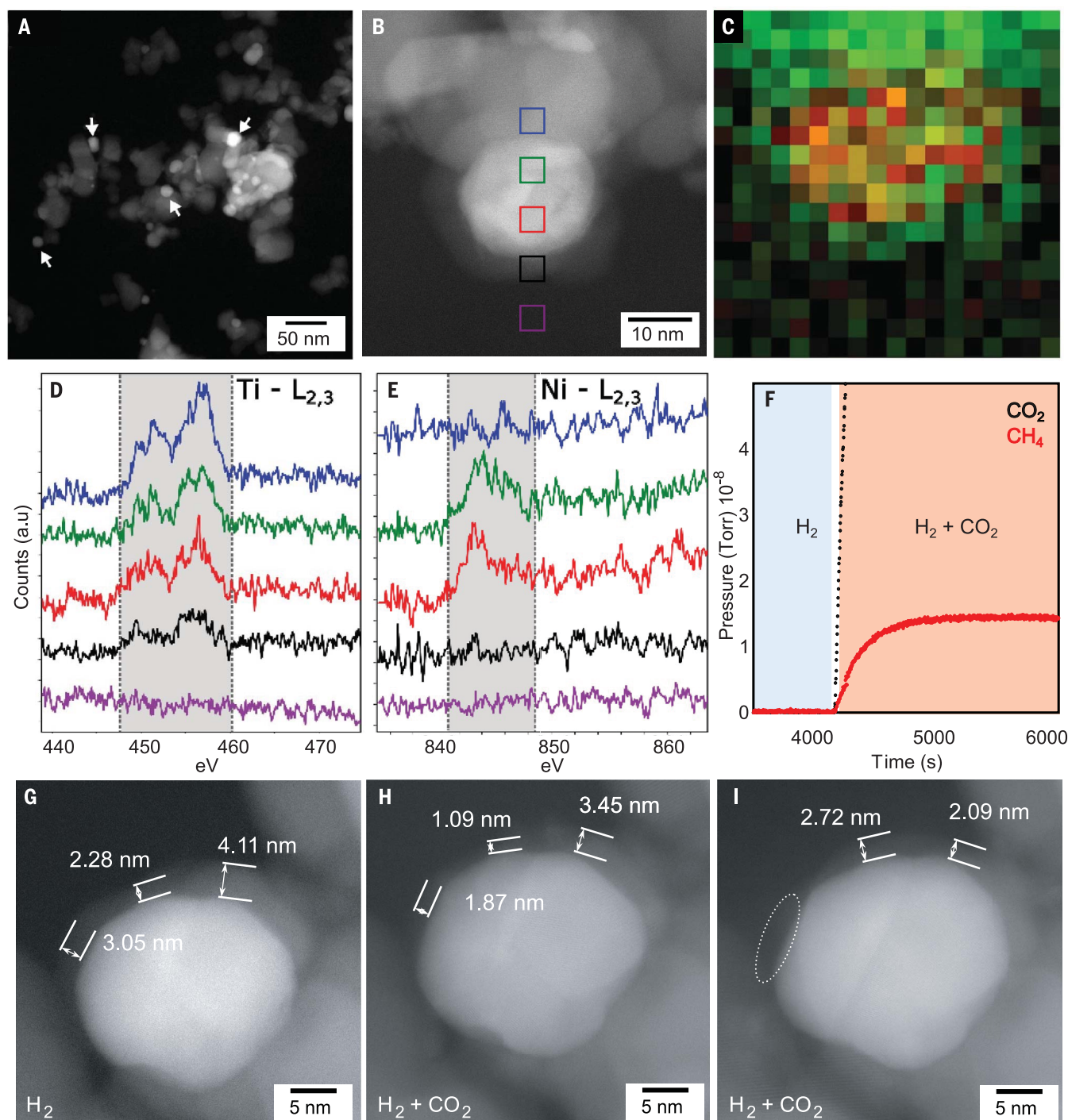


**Fig. 2. Formation of stable  $\text{TiO}_x/\text{Ni}$  overlayers during  $\text{CO}_2$  methanation on a  $\text{Ni}/\text{TiO}_2$  hydrogenation catalyst first reduced at high temperature.**

(A) HAADF-STEM overview images of  $\text{Ni}/\text{TiO}_2$  catalyst prepared in situ at  $600^\circ\text{C}$  ( $600\text{-Ni}/\text{TiO}_2$ ), where white arrows highlight the Ni NPs upon the  $\text{TiO}_2$  support. (B) High-resolution HAADF-STEM image of  $\text{Ni}/\text{TiO}_2$  catalyst in  $\text{H}_2$  at  $600^\circ\text{C}$  showing a Ni NP encapsulated in a thick  $\text{TiO}_x$  shell. Colored squares correspond to the location where EELS spectra in (D) and (E) were acquired. (C) Core loss EELS map of  $\text{Ti L}_{2,3}$  (green) and  $\text{Ni-L}_{2,3}$  (red) ionization edges. (D and E) Core loss  $\text{Ti L}_{2,3}$  (D) and  $\text{Ni L}_{2,3}$  (E) spectra showing several regions of interests within the encapsulated NP, where spectrum color indicates the location of pixels shown in (B). (F) MS data acquired at  $400^\circ\text{C}$  showing

the partial pressure of  $\text{CO}_2$  (black) and  $\text{CH}_4$  (red) for  $\text{Ni}/\text{TiO}_2$  catalysts prepared at  $600^\circ\text{C}$ , with the regions highlighted in light blue and pink corresponding to the  $\text{H}_2$  and  $\text{CO}_2/\text{H}_2$  environments, respectively. (G) High-resolution HAADF-STEM image of an individual Ni NP in  $\text{H}_2$  at  $600^\circ\text{C}$  before  $\text{CO}_2$  hydrogenation. (H) High-resolution HAADF-STEM image of the same particle as in (G) upon exposure to a  $\text{CO}_2/\text{H}_2$  ( $0.25\text{ bar CO}_2$ :  $0.75\text{ bar H}_2$ ) mixture at  $400^\circ\text{C}$  showing only partial restructuring of the thick  $\text{TiO}_x$  shell. (I) HAADF-STEM image of the same particle as in (G) and (H) upon longer exposure to a  $\text{CO}_2/\text{H}_2$  ( $0.25\text{ bar CO}_2$ :  $0.75\text{ bar H}_2$ ) mixture at  $400^\circ\text{C}$  showing further restructuring of the thick  $\text{TiO}_x$  shell and reexposure of the Ni surface, highlighted by the white circle.

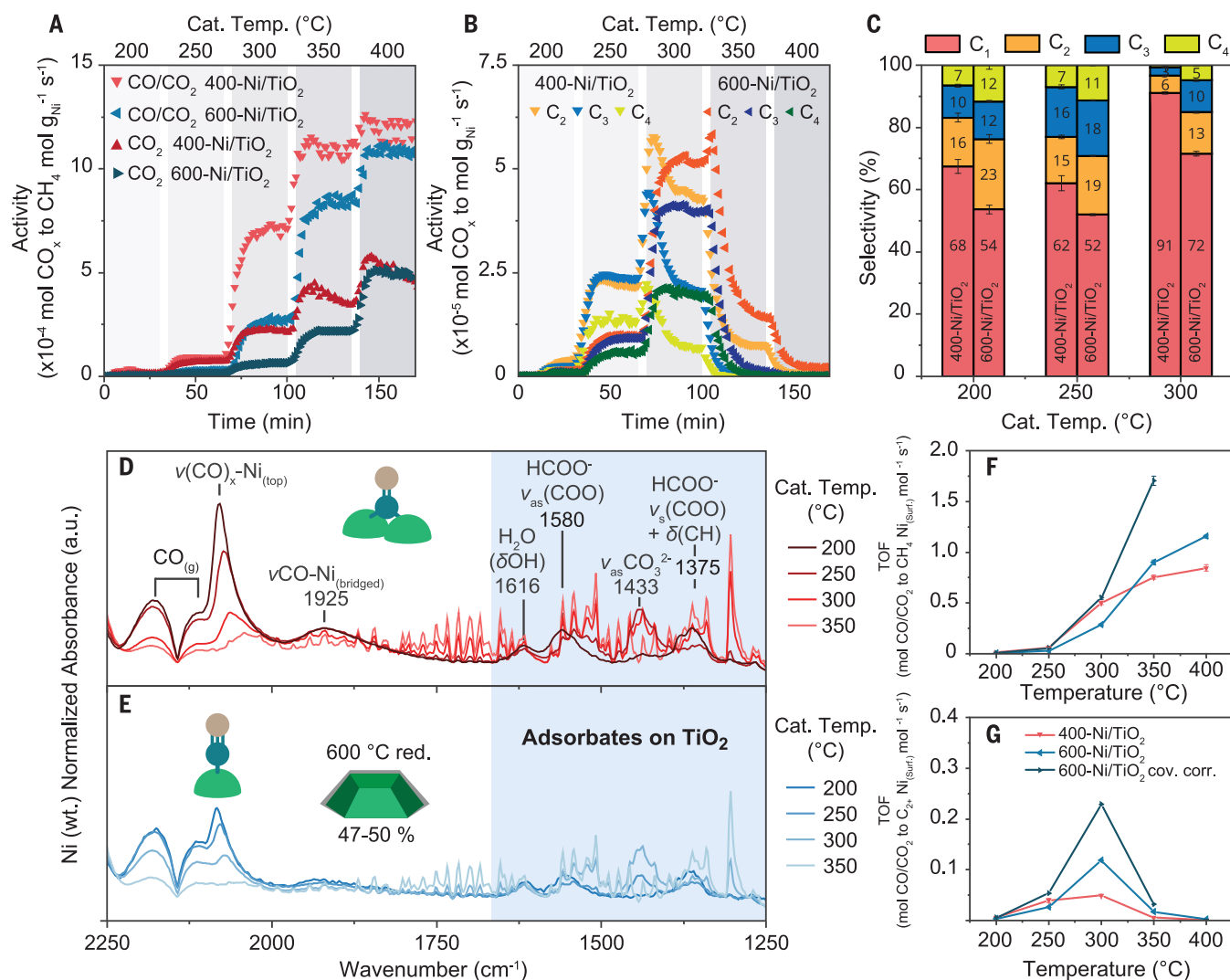


**Fig. 3. Ni/TiO<sub>2</sub> reexposure under CO and CO<sub>2</sub> hydrogenation conditions revealed by operando vibrational spectroscopy.** (A) Catalytic activity of 400-Ni/TiO<sub>2</sub> (red) and 600-Ni/TiO<sub>2</sub> (blue), normalized per gram of Ni, for CO<sub>2</sub> (dark shade) and CO/CO<sub>2</sub> methanation (light shade). (B) C-C coupling activity of 400-Ni/TiO<sub>2</sub> and 600-Ni/TiO<sub>2</sub> normalized per gram of Ni, during CO/CO<sub>2</sub> hydrogenation. (C) Selectivity to hydrocarbons in the CO/CO<sub>2</sub> hydrogenation reaction over 400-Ni/TiO<sub>2</sub> and 600-Ni/TiO<sub>2</sub>. (D and E) Operando FTIR spectra collected at 200° to 300°C under CO/CO<sub>2</sub> hydrogenation conditions over 400-Ni/TiO<sub>2</sub> (D) and 600-Ni/TiO<sub>2</sub> (E) showing Ni exposure in both catalysts. The

estimate for Ni coverage for 600-Ni/TiO<sub>2</sub> and the majority CO<sub>ads</sub> species at 300°C is schematically depicted for the two catalysts (see the supplementary materials for details). (F and G) TOF for methane production (F) and C-C coupling products (G) over 400-Ni/TiO<sub>2</sub> (red) and 600-Ni/TiO<sub>2</sub> (light blue). The dark blue line shows the TOF corrected for the most conservative estimate of exposed Ni surface in 600-Ni/TiO<sub>2</sub> (see the supplementary materials for details). Conditions for CO<sub>2</sub> methanation: CO<sub>2</sub>:H<sub>2</sub>:He = 1:4:5, 5 bar, gas hourly space velocity (GHSV) = 80,000 hours<sup>-1</sup>. Conditions for CO/CO<sub>2</sub> methanation: CO<sub>2</sub>:CO:H<sub>2</sub>:He = 3:1:7:9, 5 bar, GHSV = 80,000 hours<sup>-1</sup>.

positions in the Ni lattice were determined, from which we calculated a strain map (Fig. 1D and figs. S15 and S16). This quantitative analysis revealed an increase in tensile strain at the exposed (100) surface facet, as expected from the increased mobility of surface adatoms. By contrast, both (111) facets covered by a TiO<sub>x</sub> bilayer displayed a small negative (compressive) strain over the surface and the second atomic subsurface layer as Ni accommodated the Ni-Ti interface. A compressive strain of Ni atoms at the TiO<sub>x</sub>/Ni(111) interface was also predicted by DFT calculations for different TiO<sub>x</sub>/Ni models (tables S3 and S4).

The interatomic Ti-Ti and Ni-Ti distances were measured using the atomic positions deduced by our statistics-based approaches and found to be  $2.95 \pm 0.01$  and  $2.93 \pm 0.09$  Å, respectively. The Ti-Ti distances showed a range of 2.77 to 2.95 Å for several measured rutile (110) *d* spacing (Fig. 1D and fig. S10). This Ti-Ti distance is also consistent with continuous TiO<sub>x</sub> overlayers previously reported (13), and we anticipate that the observed compression was partially caused by the dis-

crete and minimal secondary layer of Ti atoms that was too small to arrange perfectly, as would be expected for a bulk phase-idealized crystal structure. The identity of the TiO<sub>x</sub> overlayer was further distinguished from a NiO<sub>x</sub> overlayer through in situ electron energy-loss spectroscopy (EELS) analysis (fig. S18). Similar observations were made regardless of which crystal structure (rutile or anatase) the Ni nanoparticle resided on (fig. S19).

To better understand our finding of the selective coverage of Ni(111) facets by bilayers of TiO<sub>2</sub> rutile (110), we calculated the relative stability of TiO<sub>2</sub> overlayers on the most observed

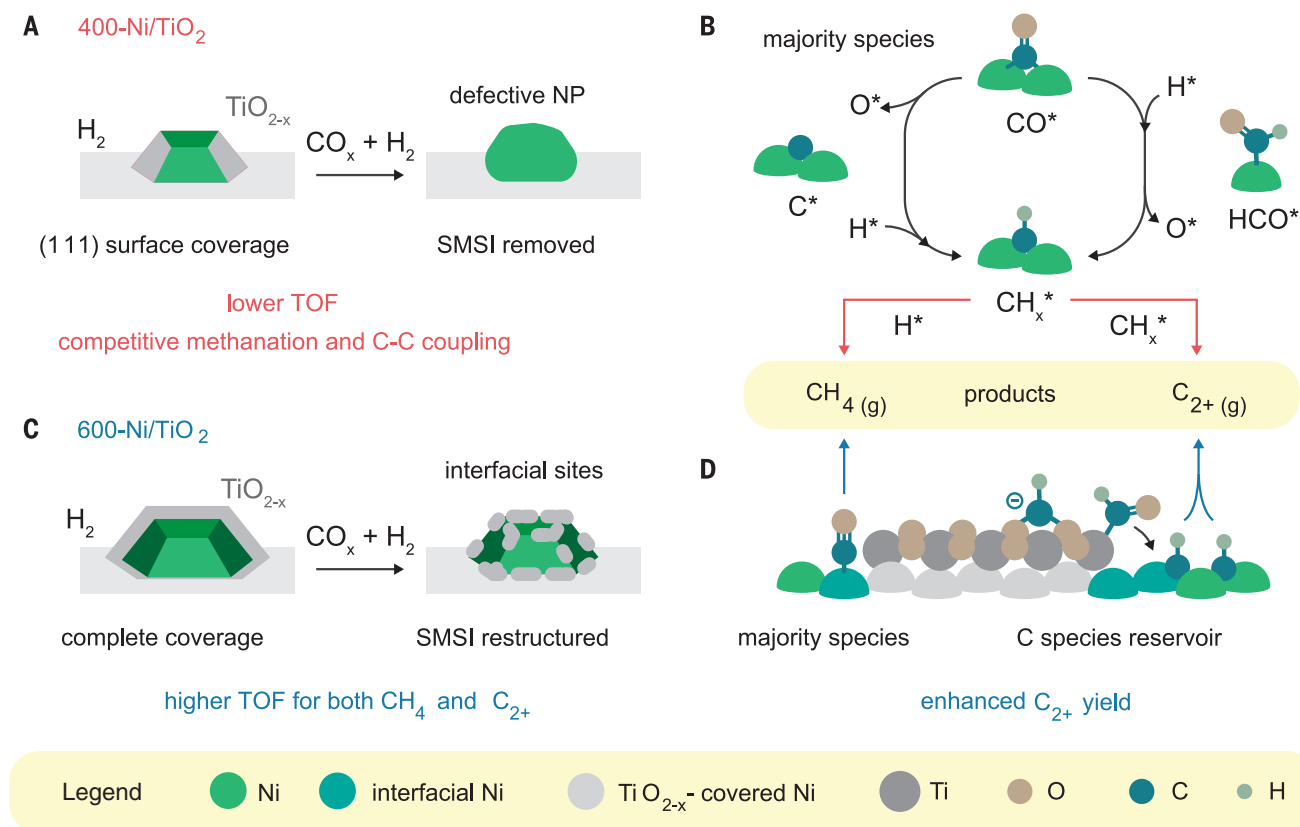


**Fig. 4. New understanding of Ni/TiO<sub>2</sub> catalyst performance and evolution during reduction and reaction.** Model for TiO<sub>x</sub> overlayer formation after 400 and 600°C reduction and restructuring under reaction conditions, which explains the observed catalytic and spectroscopic results. **(A)** 400°C reduction leads to the formation of a TiO<sub>x</sub> bilayer that is completely removed under reaction conditions, resulting in defective Ni particles. **(B)** For these particles, CO can adsorb on bridge sites (majority species). The adsorbed CO\* is converted to CH<sub>x</sub>\* through either HCO\* (H-assisted dissociation) or C\* (direct dissociation).

This species is in turn converted to methane by hydrogenation (reaction with H\*) or to C–C coupling products (C<sub>2+</sub>) by reaction with CH<sub>x</sub>\* adsorbates. **(C)** 600°C reduction leads to complete Ni coverage by TiO<sub>x</sub>, which restructures under reaction conditions. **(D)** On these particles, interfacial Ni–TiO<sub>x</sub> sites form, upon which C species from the support are brought in contact with C species on Ni, favoring C–C coupling. Furthermore, CO is preferentially bound linearly, which explains the higher TOF per active site in the catalytic methanation of CO and CO<sub>2</sub>.

Ni facets using DFT (figs. S20 and S21). Based on the quantitative structural analysis of the atomic resolution in situ HAADF-STEM data, we built TiO<sub>2</sub>/Ni models using a Ni slab of four atomic layers oriented along the (111), (100), and (110) facets covered by two monolayers of rutile (110) (see the “Computational details” section in the supplementary materials). The lattice mismatch between the TiO<sub>2</sub> rutile structure and the Ni surfaces would induce strain. After energy minimization, we found the strain energies for the Ni(111) and Ni(100) surfaces to be 0.5 and 3.1 kJ/mole of TiO<sub>2</sub>, respectively. This difference was consistent with the distortion and irregularity of the modeled TiO<sub>2</sub> overlayer on Ni(100) (Fig. 1E and fig. S20). The lower energy toll calculated for the formation of TiO<sub>2</sub> overlayers on Ni(111) thus explains the experimentally observed facet-selective coverage of Ni NPs.

To further investigate the structure of the TiO<sub>x</sub>/Ni(111) interface, we used different configurations as input for computational calculations, varying the type and number of atoms

between the interfacial Ni and TiO<sub>x</sub> layers (figs. S20 and S21). When the Ni surface was covered with a TiO<sub>2</sub> rutile (110), the computed Ni–Ti interlayer distance was 3.20 Å, which is larger than what was experimentally observed (2.80 to 3.00 Å; Fig. 1E, top). Conversely, a Ni–Ti distance of 2.79 Å was calculated for a partially reduced overlayer, where interfacial oxygen atoms were replaced by H atoms, and H\* atoms were adsorbed on the Ni surface. On the basis of these calculations, the overlayers are most likely a suboxide phase.

Because in situ HAADF-STEM imaging provided only local information on single NPs, we performed H<sub>2</sub> chemisorption to estimate the bulk average percentage of exposed Ni surface for the ensemble of Ni NPs after the reduction of Ni/TiO<sub>2</sub> (fig. S23). The amount of chemisorbed H<sub>2</sub> for 400-Ni/TiO<sub>2</sub> was 32 μmol/g, which corresponds to 6.7% of the total number of Ni atoms, or an apparent average NP size of 15 nm, assuming a 1:1 H:Ni stoichiometry. The apparent Ni NP size calculated from H<sub>2</sub> chemisorption was substan-

tially larger than that measured with TEM (5.3 to 7.5 nm; Fig. 1B and figs. S4, S5, and S7), indicating that part of the surface of Ni was blocked and not accessible to the gas phase. If no chemisorption took place on the TiO<sub>x</sub> overlayers, then there was a 25 to 46% surface coverage of Ni by TiO<sub>x</sub> in 400-Ni/TiO<sub>2</sub>. This value is in agreement with the fraction of Ni(111) surface sites (35 to 57%) predicted for Wulff-constructed Ni NPs of such sizes, (27) as well as with the in situ HAADF-STEM evidence of selective encapsulation of Ni(111) facets.

#### Ni reexposure during CO<sub>2</sub> hydrogenation for Ni/TiO<sub>2</sub> after 400°C reduction

We followed changes in the TiO<sub>x</sub> overlayer under CO<sub>2</sub> hydrogenation reaction conditions by tracking a single Ni NP with HAADF-STEM while switching from H<sub>2</sub> to CO<sub>2</sub>:H<sub>2</sub> at 400°C and atmospheric pressure. Reactant and product gases from the windowed gas cell were tracked in real time during the reaction using mass spectrometry (MS) (Fig. 1H and fig. S24). Upon introduction of the CO<sub>2</sub>:H<sub>2</sub> mixture, there



was detectable formation of CH<sub>4</sub>, confirming that the catalyst actively performed CO<sub>2</sub> hydrogenation during observation within the electron microscope. As observed for other NPs (figs. S12 and S13), the Ni NP shown in Fig. 1C developed a TiO<sub>x</sub> overlayer that selectively occupied Ni's (111) surface facets before hydrogenation.

Upon CO<sub>2</sub> exposure at 400°C, the same Ni NP restructured and lost a large proportion of its highly faceted surface, with only a small percentage of the Ni(100) facet remaining. The NP exhibited an overall rounded morphology and retained its Ni metallic phase (Fig. 1F and figs. S25 and S26). Comparative strain maps calculated for the same NP during CO<sub>2</sub> hydrogenation showed an increase in tensile strain over the entire NP surface in both the x- and y-directions and a loss in compressive strain (Fig. 1G). We attributed these changes to the loss of the Ni-Ti interface during hydrogenation, which resulted in lower atomic coordination and higher mobility of surface atoms compared with its TiO<sub>2</sub>-encapsulated counterpart (400-Ni/TiO<sub>2</sub>; Fig. 1, C and D). The supported Ni catalyst dynamically evolved to express its more-active facets during CO/CO<sub>2</sub> hydrogenation (28). Thermodynamic calculations by the Gibbs free energy minimization method showed that TiO<sub>x</sub> became unstable under CO<sub>2</sub> hydrogenation conditions (table S6; see the supplementary materials for details), which suggests that the removal of the TiO<sub>x</sub> overlayer was induced by changes in chemical potential and not by the Ni NP restructuring.

To show that such removal of TiO<sub>x</sub> overlayer upon exposure to CO<sub>2</sub> hydrogenation conditions is representative of the bulk of the sample, we measured the attenuation of Ni 2p signal relatively to Ti 2p signals in NAP-XPS, which provided indirect evidence for encapsulation (fig. S27). A fresh Ni/TiO<sub>2</sub> catalyst was reduced at 400°C in situ at 0.3 mbar H<sub>2</sub> and then exposed to cycles of 0.3 mbar H<sub>2</sub> + 0.3 mbar CO<sub>2</sub> and pure H<sub>2</sub>. This sequence resulted in a reversible change of the Ni/Ti signal ratio that was consistent with the exposure and coverage of Ni under CO<sub>2</sub> hydrogenation reaction conditions and H<sub>2</sub>, respectively (fig. S29; see the supplementary materials for details).

### TiO<sub>x</sub> overlayer formation and restructuring for 600°C reduced Ni/TiO<sub>2</sub>

With the aim of forming a more-stable TiO<sub>x</sub> overlayer that would survive CO<sub>2</sub> hydrogenation conditions, we reduced the 6 wt % Ni/TiO<sub>2</sub> catalyst in situ at 600°C (600-Ni/TiO<sub>2</sub>). Compared with the Ni/TiO<sub>2</sub> catalyst prepared at 400°C (400-Ni/TiO<sub>2</sub>), the NP diameter approximately doubled to 14.0 nm (±4.0 nm size distribution) for the 600-Ni/TiO<sub>2</sub> (Fig. 2A and figs. S6 and S7). The larger NP diameter is the result of the higher reduction temperature and is consistent with TEM and XRD observa-

tions after ex situ reduction (tables S1 and S2 and figs. S6 to S8). 600-Ni/TiO<sub>2</sub> displayed a completely encapsulating and relatively thick (1 to 2 nm) TiO<sub>x</sub> overlayer (Fig. 2B and fig. S30). The greater degree of encapsulation occurred with the higher temperature treatment because the partial reduction of TiO<sub>2</sub> that is needed to form the TiO<sub>x</sub> overlayers is favored at higher temperatures (figs. S2 and S3). Because of the lack of a single crystalline layer, atomic-resolution HAADF-STEM was not applicable. Therefore, the formation of a TiO<sub>x</sub> overlayer was corroborated by in situ EELS analysis, which showed a Ti L<sub>2,3</sub> ionization edge signal throughout the entire Ni NP (Fig. 2, B to E, and figs. S31 to S33). Consistent with the complete encapsulation by TiO<sub>x</sub> observed by electron microscopy, H<sub>2</sub> chemisorption was almost completely suppressed for the 600-Ni/TiO<sub>2</sub> catalysts (fig. S23).

After reduction, the in situ-prepared 600-Ni/TiO<sub>2</sub> catalyst was exposed to CO<sub>2</sub> hydrogenation reaction conditions at 400°C. Similar to the 400-Ni/TiO<sub>2</sub>, CO<sub>2</sub> methanation was confirmed by tracking reactant and product gases by MS (Fig. 2F). Figure 2, G to I, shows the same Ni NP under H<sub>2</sub> (Fig. 2G) and under a CO<sub>2</sub>:H<sub>2</sub> mixture (Fig. 2, H and I) at atmospheric pressure. The TiO<sub>x</sub>-suboxide overlayer was still visible but became more inhomogeneous after CO<sub>2</sub> exposure compared with the pristine catalyst, indicating its partial degradation. Shell thickness measurements in Fig. 2, G to I, show the regions in which most changes in coverage were observed, with a circle identifying an area of the Ni surface that no longer appeared to be encapsulated by the overlayer (fig. S34; see the supplementary materials for details).

Such overlayers survived even exposure to pure CO<sub>2</sub> at 400°C (fig. S34), in contrast to the easily removed TiO<sub>x</sub> bilayer observed for 400-Ni/TiO<sub>2</sub> catalysts. We hypothesize that the different stability is caused by the greater thickness of the shell, which contained sufficient Ti atoms to form stable patches of TiO<sub>x</sub> on Ni. Despite the extended encapsulation, the catalyst was active for the CO<sub>2</sub> hydrogenation reaction to methane, as shown by online MS analysis (Fig. 2F and fig. S24).

Our operando STEM results suggest that 600-Ni/TiO<sub>2</sub> remained predominantly encapsulated by TiO<sub>x</sub> under CO<sub>2</sub> hydrogenation reaction conditions. Therefore, we expected to observe an almost complete loss of activity for such catalysts in reactions promoted by Ni. However, both the 400- and 600-Ni/TiO<sub>2</sub> catalysts were active for CO<sub>2</sub> hydrogenation during operando STEM experiments (Figs. 1H and 2F).

### Comparison of catalytic performance

To investigate the effect of the residual TiO<sub>x</sub> overlayer on the catalytic CO/CO<sub>2</sub> hydrogenation

performance of Ni/TiO<sub>2</sub> catalysts, we performed catalytic tests on 20 mg of catalysts in operando Fourier transform infrared (FTIR) spectroscopy experiments under hydrogenation conditions. These experiments showed that both catalysts were active for CO<sub>2</sub> hydrogenation at 200° to 400°C and 5 bar (Fig. 3A and figs. S35 to S38), in agreement with operando TEM MS measurements. Compared with 400-Ni/TiO<sub>2</sub>, 600-Ni/TiO<sub>2</sub> showed a decrease in overall catalytic activity per gram of Ni, but a higher stability (Fig. 3A), and higher C<sub>2+</sub> selectivity (figs. S36 and S37). All operando FTIR spectroscopy and catalytic results reported herein were repeated on two separate batches of Ni/TiO<sub>2</sub> catalysts, showing comparable figures and trends (figs. S45 to S50).

The enhancement in C<sub>2+</sub> selectivity for the 600-Ni/TiO<sub>2</sub> catalyst became even more evident in CO/CO<sub>2</sub> cohydrogenation experiments, with a C<sub>2+</sub> selectivity of 28 and 9% for 600- and 400-Ni/TiO<sub>2</sub> catalysts, respectively, at 300°C and 5 bar pressure (Fig. 3, A to C). These results further indicate that under reaction conditions, the Ni surface in 600-Ni/TiO<sub>2</sub> was partially reexposed, and that this affected the product selectivity of the reaction. Accordingly, ex situ Ni 2p XPS spectra of the used 600-Ni/TiO<sub>2</sub> catalyst (after one reaction cycle, as in Fig. 3A) showed a higher Ni signal intensity than the reduced 600-Ni/TiO<sub>2</sub>, further supporting Ni reexposure under reaction conditions (fig. S27).

To provide direct evidence for the reexposure of the Ni surface under reaction conditions and to quantify the number of exposed sites, we performed operando FTIR spectroscopy experiments during CO/CO<sub>2</sub> cohydrogenation (Fig. 3, D and E) and CO<sub>2</sub> hydrogenation (fig. S38). The 400- and 600-Ni/TiO<sub>2</sub> catalysts showed similar CO<sub>x</sub> hydrogenation intermediate signals, but with different relative intensities: CO<sub>(g)</sub> bands were observed in the region 2250 to 2100 cm<sup>-1</sup>, followed by relatively sharp bands at 2078 to 2062 cm<sup>-1</sup> (peak positions depended on temperature; figs. S40 and S41), which we ascribed to adsorbed sub-carbonyl Ni (CO)<sub>x</sub> (with x = 2,3) species (29–31). Ni(CO)<sub>4</sub> formation under the conditions of this study was ruled out by thermodynamic calculations (table S7). A component corresponding to Ni-CO<sub>top</sub> was observed in the spectral region between 2060 and 2032 cm<sup>-1</sup>, whereas bridged CO (CO<sub>br</sub>) adsorbed on Ni was observed in the spectral region between 1920 and 1940 cm<sup>-1</sup>. A series of bands at lower wave numbers were ascribed to adsorbates on TiO<sub>2</sub>, because they were also present over the pure support {fig. S42: adsorbed water peaks at 1616 cm<sup>-1</sup> [δ (OH)]; formate [HCOO<sup>-</sup>] peaks at 1580 and 1375 cm<sup>-1</sup>; and carbonates [CO<sub>3</sub><sup>2-</sup>] peak at 1433 cm<sup>-1</sup> (32)}.

Because the bands of adsorbed CO species (2078 to 1750 cm<sup>-1</sup>) were absent over pure TiO<sub>2</sub> under the same reaction conditions (fig.

S42), these spectral features were taken as a measure of the extent of Ni surface exposure under reaction conditions. Assuming complete reexposure of 400-Ni/TiO<sub>2</sub> under reaction conditions, as evidenced by TEM (Fig. 1F and fig. S26), the integration of the CO bands for 400- and 600-Ni/TiO<sub>2</sub> revealed a TiO<sub>x</sub> coverage of ~ 50% for 600-Ni/TiO<sub>2</sub>, decreasing with increasing reaction temperature (table S5). These results, combined with the STEM results shown in Fig. 2, G to I, provided evidence for a reexposed Ni surface, partially covered by TiO<sub>x</sub> agglomerates, that remained on the Ni NP surfaces.

Taking into account such a fraction of exposed Ni surface derived by operando FTIR spectroscopy, we calculated exposure-corrected turnover frequencies (TOFs) for methanation and C–C coupling (Fig. 3, F and G, and figs. S43 and S44; see the supplementary materials for details). Although the geometrical (i.e., not corrected by coverage) TOFs of 400- and 600-Ni/TiO<sub>2</sub> were comparable, the exposure-corrected TOFs of 600-Ni/TiO<sub>2</sub> were higher, indicating that the reexposed Ni sites had a higher specific activity for both methanation and C–C coupling.

### Mechanistic insights and structure sensitivity

On the basis of our results, we propose a model of the restructured Ni/TiO<sub>2</sub> catalysts under reaction conditions to explain changes in surface chemistry and, ultimately, in catalyst performance. The higher methanation TOF for 600-Ni/TiO<sub>2</sub> may be explained by a change in most of the CO<sub>ads</sub> species, from less-active, bridged CO<sub>ads</sub> for 400-Ni/TiO<sub>2</sub> (Fig. 4, A and B) to more active, linear CO<sub>ads</sub> for 600-Ni/TiO<sub>2</sub> (Fig. 4, C and D, and fig. S40B) (28). Because Ni NPs were larger in the 600-Ni/TiO<sub>2</sub> catalyst, and more extended Ni surfaces should result in more bridged CO<sub>ads</sub> (33), this observation can best be explained by the formation of a patchy TiO<sub>x</sub> overlayer that increased the extent of the Ni–TiO<sub>x</sub> interface and led to fewer available sites for CO<sub>bridge</sub> formation, even on extended surfaces. Similarly, the enhancement in CO hydrogenation TOF on Pt/TiO<sub>2</sub> catalysts was caused by cooperative adsorption of CO at the interface, with the C atom coordinated to Pt and oxygen on the oxygen-deficient TiO<sub>x</sub> (34). The formation of such structures was shown by the combination of operando FTIR spectroscopy and HAADF-STEM results (Figs. 2 and 3). In the case of the 400-Ni/TiO<sub>2</sub>, the interface among Ni, TiO<sub>2</sub>, and the gas phase is instead limited to the perimeter of the NP in contact with the support because of the complete removal of the TiO<sub>x</sub> overlayers under reaction conditions.

The higher C–C coupling TOF for 600-Ni/TiO<sub>2</sub> was also in contrast with previous observations on Ni/SiO<sub>2</sub> catalysts, where C–C coupling was anticorrelated with methanation

activity, because it was limited by the high hydrogenation rate of CH<sub>x</sub>\* (x = 0 to 3) adsorbates on Ni. Both C–C coupling and methanation having higher TOF for 600-Ni/TiO<sub>2</sub> suggested that an alternative pathway was available for C–C coupling in the presence of a patchy TiO<sub>x</sub> overlayer. We propose that the increased Ni–TiO<sub>x</sub> interface aided C–C coupling by providing a reservoir of C species in close contact with adsorbates on Ni and by stabilizing intermediates and transition states (Fig. 4D). Accordingly, calculations on TiO<sub>x</sub>/Ni catalysts showed that CO activation and CH–CH coupling were both more favorable at interfacial Ni–TiO<sub>x</sub> sites (35). An alternative explanation for enhanced C–C coupling would involve reverse H spillover from Ni to TiO<sub>x</sub>, hindering hydrogenation of CH<sub>x</sub>\* adsorbates by H\*. However, this mechanism is not consistent with the observed higher methanation TOF, which requires H\*. Ex situ XRD showed no extended TiO<sub>2</sub> phase transformation, such as from anatase to rutile, at 600°C (fig. S9) that could have affected the catalytic activity (36), although further studies are required to substantiate this explanation.

### Discussion

The observed restructuring of TiO<sub>x</sub> overlayer under reaction conditions was consistent with recent observations on Pt/TiO<sub>2</sub> by in situ TEM during reduction-oxidation-reduction cycles at 600°C, in which oxidative treatments cause amorphous TiO<sub>2</sub> islands to form, reexposing part of the metal surface (10). CO/CO<sub>2</sub> hydrogenation conditions were sufficiently oxidative to shift the thermodynamic equilibrium to TiO<sub>2</sub> (table S6). Our results show that, kinetically, a (partial) removal and restructuring of TiO<sub>x</sub> overlayers could occur even at temperatures as low as 200°C, reexposing the active Ni surface.

Both CO and CO<sub>2</sub> hydrogenations are structure-sensitive reactions (33, 37), meaning that the TOF in the reactions changes as a function of NP size (38). Nonetheless, structure sensitivity only resulted in lower TOF for NPs with diameters below 2 to 4 nm, well below the range considered in this study (28, 37). Conversely, NPs with larger sizes have been reported to have similar, or even smaller, TOF, which would make the effect of SMSI in TOF enhancement even greater (33). Finally, C–C coupling was not strongly structure sensitive, according to theoretical calculations on Ni surfaces (28). Thus, the current observations that the TOF of both methanation and C–C coupling increase with Ni NP size could not possibly be explained by classical structure sensitivity concept, which only accounts for Ni surface sites variation with NP size (39). Similar deviations from classical structure sensitivity were observed for Co-based catalysts in CO<sub>2</sub> hydrogenation, where partially reduced cobalt oxide covered with metallic

clusters of a few Co atoms showed substantially higher intrinsic activity caused by interfacial effects (40).

In summary, here, we directly observed for the first time the restructuring of metal oxide overlayers under operating conditions and rationalized their effects on the activity and selectivity of Ni in CO/CO<sub>2</sub> hydrogenation reactions depending on the reduction temperature. A similar, although rudimentary, model of highly active interfacial sites was proposed by Burch *et al.* in the 1980s to explain the higher activity of Ni/TiO<sub>2</sub> compared with Ni/SiO<sub>2</sub> on the basis of chemisorption results alone (41). Evidence that overlayers may be stabilized under reaction conditions was reported for Rh/TiO<sub>2</sub> catalysts, where pretreatments in CO<sub>2</sub>-rich atmospheres lead to the formation of a more-persistent, “adsorbate-induced” SMSI (14). Recently, the enhancement of activity in methanol steam-reforming reaction was also correlated with the amount of Cu–ZnO<sub>x</sub> interfacial sites (albeit observed ex situ), exhibiting faster kinetics for \*CH<sub>3</sub>O dehydrogenation and H<sub>2</sub>O dissociation (8). We now provide operando evidence for the formation of Ni–TiO<sub>x</sub> interfacial sites and show their effect on catalytic performance. A similar operando approach could be applied to understand many other chemical reactions in which the proximity of the active phase and support or promoters has been found to be essential for higher activity or better selectivity, such as olefins production over Fe-based catalysts promoted by K (42), CO oxidation over Pd/CeO<sub>2</sub> (43), or propane dehydrogenation over Pt/Sn/CeO<sub>2</sub> (44). Crucial in this endeavor will be the simultaneous measurement of catalytic performance and the monitoring and control of the support, such as crystal phase, porosity, oxidation state, and exposed facets, and of the supported active phase nanostructure, such as NP size, shape, and composition.

### REFERENCES AND NOTES

1. C. Vogt *et al.*, *Nat. Commun.* **12**, 7096 (2021).
2. A. V. Puga, *Catal. Sci. Technol.* **8**, 5681–5707 (2018).
3. S. B. Vendelbo *et al.*, *Nat. Mater.* **13**, 884–890 (2014).
4. S. J. Tauster, S. C. Fung, R. L. Garten, *J. Am. Chem. Soc.* **100**, 170–175 (1978).
5. M. Tang *et al.*, *Angew. Chem. Int. Ed.* **60**, 22339–22344 (2021).
6. C. Wu *et al.*, *Nat. Commun.* **11**, 5767 (2020).
7. S. Samira *et al.*, *JACS Au* **1**, 2224–2241 (2021).
8. D. Li *et al.*, *Nat. Catal.* **5**, 99–108 (2022).
9. M. Macino *et al.*, *Nat. Catal.* **2**, 873–881 (2019).
10. A. Beck *et al.*, *Nat. Commun.* **11**, 3220 (2020).
11. C. Hernández Mejía, T. W. van Deelen, K. P. de Jong, *Nat. Commun.* **9**, 4459 (2018).
12. H. Frey, A. Beck, X. Huang, J. A. van Bokhoven, M. G. Willinger, *Science* **376**, 982–987 (2022).
13. S. Zhang *et al.*, *Nano Lett.* **16**, 4528–4534 (2016).
14. J. C. Matsubu *et al.*, *Nat. Chem.* **9**, 120–127 (2017).
15. A. Bergmann, B. Roldan Cuenya, *ACS Catal.* **9**, 10020–10043 (2019).
16. X. Zhang *et al.*, *Nat. Catal.* **3**, 411–417 (2020).
17. S. W. Chee, T. Lunkenbein, R. Schlögl, B. R. Cuenya, *J. Phys. Condens. Matter* **33**, 153001 (2021).
18. A. S. Kashin, V. P. Ananikov, *Nat. Rev. Chem.* **3**, 624–637 (2019).

19. S. Hwang, X. Chen, G. Zhou, D. Su, *Adv. Energy Mater.* **10**, 1902105 (2020).
20. X. Zhang *et al.*, *ACS Catal.* **9**, 3551–3563 (2019).
21. A. Dokania, A. Ramirez, A. Bavykina, J. Gascon, *ACS Energy Lett.* **4**, 167–176 (2019).
22. M. Li *et al.*, *ACS Appl. Energy Mater.* **4**, 12326–12335 (2021).
23. T. Altantzis *et al.*, *Nano Lett.* **19**, 477–481 (2019).
24. A. De Backer, G. T. Martinez, A. Rosenauer, S. Van Aert, *Ultramicroscopy* **134**, 23–33 (2013).
25. J. Fatermans, S. Van Aert, A. J. den Dekker, *Ultramicroscopy* **201**, 81–91 (2019).
26. J. Fatermans *et al.*, *Phys. Rev. Lett.* **121**, 056101 (2018).
27. E. B. Sterk *et al.*, *JACS Au* **2**, 2714–2730 (2022).
28. C. Vogt *et al.*, *Nat. Commun.* **10**, 5330 (2019).
29. K. Hadjiivanov *et al.*, *J. Catal.* **185**, 314–323 (1999).
30. M. Agnelli, H. M. Swaan, C. Marquez-Alvarez, G. A. Martin, C. Mirodatos, *J. Catal.* **175**, 117–128 (1998).
31. C. Hernández Mejía, C. Vogt, B. M. Weckhuysen, K. P. de Jong, *Catal. Today* **343**, 56–62 (2020).
32. A. Davydov, *Molecular Spectroscopy of Oxide Catalyst Surfaces* (Wiley, 2003).
33. C. Vogt *et al.*, *Nat. Catal.* **1**, 127–134 (2018).
34. B. Cornils, W. A. Herrmann, J.-H. Xu, H.-W. Zanthoff, *Catalysis from A to Z: A Concise Encyclopedia* (Wiley, 5th ed., 2020).
35. M. Xu *et al.*, *Nat. Commun.* **13**, 6720 (2022).
36. D. A. H. Hanaor, C. C. Sorrell, *J. Mater. Sci.* **46**, 855–874 (2011).
37. G. L. Bezemer *et al.*, *J. Am. Chem. Soc.* **128**, 3956–3964 (2006).
38. R. A. Van Santen, *Acc. Chem. Res.* **42**, 57–66 (2009).
39. C. Vogt, B. M. Weckhuysen, *Nat. Rev. Chem.* **6**, 89–111 (2022).
40. A. Parastaev *et al.*, *Nat. Catal.* **5**, 1051–1060 (2022).
41. R. Burch, A. R. Flambard, *J. Catal.* **78**, 389–405 (1982).
42. Y. Han *et al.*, *ACS Catal.* **10**, 12098–12108 (2020).
43. M. Cargnello *et al.*, *Science* **341**, 771–773 (2013).
44. H. Xiong *et al.*, *Angew. Chem. Int. Ed.* **56**, 8986–8991 (2017).

#### ACKNOWLEDGMENTS

B.M.W. thanks NWO for a CHIPP Research Grant, a Gravitation Program [Netherlands Center for Multiscale Catalytic Energy Conversion (MCEC)] grant, and an Advanced Research Center Chemical Building Blocks Consortium (ARC CBBC) grant. We thank S. Turner for performing the STEM measurements, L. Smulders for H<sub>2</sub> chemisorption experiments, C. Hernández Mejía for performing the TPR-TPO experiments, and J. Harmel and K. Cheng for performing the H<sub>2</sub> chemisorption measurements (all from Utrecht University). This work made use of the Dutch national e-infrastructure with the support of the SURF Cooperative using grant no. EINF-2959. **Funding:** This work was supported by BASF and NWO CHIPP (research grant to B.M.W.); the MCEC NWO Gravitation Program (B.M.W.); the ARC-CBBC NWO Program (B.M.W.); the European Research Council (grant 770887 PICOMETRICS to

S.V.A.); and the European Research Council (grant 815128 REALNANO to S.B.). **Author contributions:** Conceptualization: M.M., K.J., A.E.M.M., S.B., B.M.W.; Funding acquisition: B.M.W., S.B.; Investigation: M.M., K.J., A.E.M.M., C.V., T.D., E.G., J.N.L., W.v.d.S., B.Š.; Methodology: M.M., K.J., A.E.M.M., C.V., T.D., B.S., E.G., J.N.L., E.A.I., S.V.A., T.A.; Project administration: E.G., P.B.; Supervision: M.M., B.M.W., S.B.; Visualization: K.J., M.M., A.E.M.M., T.D., J.N.L., E.A.I.; Writing: M.M., K.J., A.E.M.M., S.B., B.M.W. **Competing interests:** The authors declare that no competing interests. **Data and materials availability:** All data needed to evaluate the conclusions in this study are present in the main text or the supplementary materials. **License information:** Copyright © 2023 the authors, some rights reserved; exclusive licensee American Association for the Advancement of Science. No claim to original US government works. <https://www.science.org/about/science-licenses-journal-article-reuse>

#### SUPPLEMENTARY MATERIALS

[science.org/doi/10.1126/science.adf6984](https://science.org/doi/10.1126/science.adf6984)

Materials and Methods

Figs. S1 to S50

Tables S1 to S11

References (45–72)

Submitted 7 November 2022; accepted 11 April 2023  
10.1126/science.adf6984